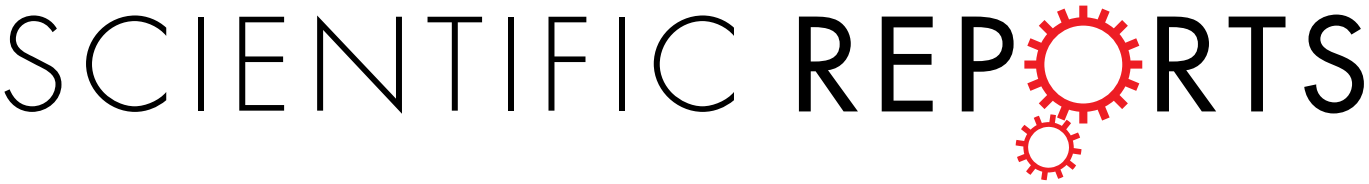

OPEN

Crack nucleation criterion and its application to impact indentation in glasses

Received: 21 October 2015
Accepted: 14 March 2016
Published: 15 April 2016

Jian Luo, K. Deenamma Vargheese, Adama Tandia, Guangli Hu & John C. Mauro

Molecular dynamics (MD) simulations are used to directly observe nucleation of median cracks in oxide glasses under indentation. Indenters with sharp angles can nucleate median cracks in samples with no pre-existing flaws, while indenters with larger indenter angles cannot. Increasing the tip radius increases the critical load for nucleation of the median crack. Based upon an independent set of simulations under homogeneous loading, the fracture criterion in the domain of the principal stresses is constructed. The fracture criterion, or "fracture locus", can quantitatively explain the observed effects of indenter angle and indenter tip radius on median crack nucleation. Our simulations suggest that beyond the maximum principal stress, plasticity and multi-axial stresses should also be considered for crack nucleation under indentation, even for brittle glassy systems.

Contact cracking is central to a wide range of engineering applications such as cutting, grinding, drilling, and fragmentation[1]. Contact induced damage is a key limiting factor of the lifetime of the brittle ceramic and glassy components[2,3]. Studies on contact mechanics date back at least one century[4], becoming especially prevalent during 1950 to 1970[5]. Recent unprecedented demands for damage resistant glasses on consumer electronic devices further stimulate the need for better understanding of contact cracking mechanism in brittle or quasi-brittle materials. At least two difficulties act to impede such progress. One lies in the fact that contact cracking happens within microseconds. In addition, the crack usually nucleates in the interior of the material. Therefore, it is generally difficult to conduct *in situ* characterization in real time experimentally to quantify the stress and strain fields and determine the criterion for fracture. Another hurdle is the complicated nature of stress/strain fields under indentation. While the elastic stress field under indentation is well-defined[5], the plastic flow, densification, and cracking under indentation profoundly complicate the stress fields and material behavior. Prominent studies have highlighted the importance of densification or shear flow in the plastic zone[6–13]. However, most of the experimental findings remain phenomenological, and existing damage models remain empirical[2,3,14]. Detailed understanding of crack nucleation mechanisms under indentation is still lacking[3,15].

Computational simulations are an important complementary tool to overcome the spatio-temporal limitations and the analytically untractable complexity when studying indentation[16]. Finite element method (FEM) is a powerful and widely-employed method to analyze indentation[17–20]. However, extreme deformation in the plastic zone and shear faults or shear bands[6,10,21,22] and non-continuity induced by cracking can cause severe numerical problems in FEM. A more fundamental limitation of FEM for the study of crack nucleation lies in the working principle that the crack nucleation criterion, as well as elasticity and plasticity, is an input to rather than an output from FEM. In other words, FEM can apply a fracture criterion to complex and large scale objects of interest, but it cannot be used to determine the fracture criterion itself.

In theory, lower level particle based simulation methods, such as first principles and molecular dynamics (MD) simulations, can output the critical fracture criterion based on fundamental physics that governs the interatomic interactions. However, first principles calculations are limited to a time-scale on the order of picoseconds and a spatial scale on the order of nanometers, rendering them impractical for the study of indentation fracture. Classical molecular dynamics simulations have been extended to submicron to micron scales[23–25] in order to calculate the criteria for fracture. However, for oxide glasses, additional computational time due to the long range Coulombic interactions severely hinders large scale simulations. As a result, most MD simulations of oxide glasses have been limited to the sample size on the order of tens of nanometers in size[26–28]. Using screened Coulombic interactions, MD simulations of oxide glasses in the submicron scale have been performed[29,30]. However, contact cracking has not hitherto been observed in MD simulation.

Science and Technology Division, Corning Incorporated, Corning, New York 14831, USA. Correspondence and requests for materials should be addressed to J.L. (email: luoj2@corning.com) or J.M. (email: mauroj@corning.com)

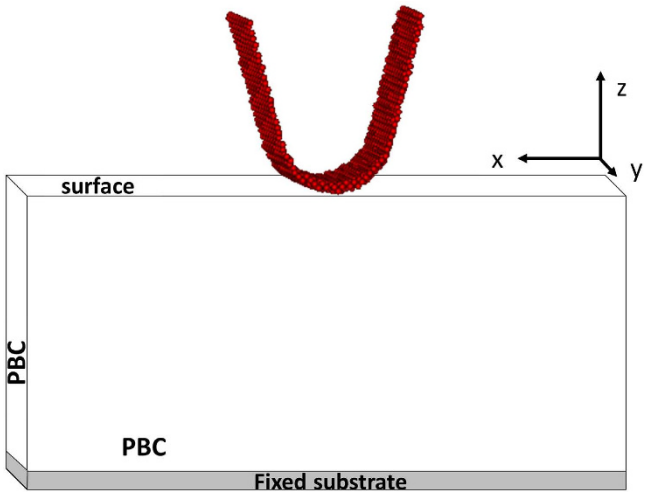

Figure 1. Indentation simulation setup. The geometry of the rigid atomic indenter is defined by the angle and tip radius. Periodic boundary condition (PBC) applies to the x and y directions. Upper-z direction is a surface. A 0.5 nm thick layer in the lower-z direction is fixed as a substrate.

In the present study, crack nucleation under impact indentation is directly captured with full atomic details through MD simulation. Indenter angle and indenter tip radius strongly affect the local stress fields and deformation mechanism. The local stress evolution is carefully examined and the critical local stress conditions for crack nucleation are captured. Combining the stress state evolution with the fracture criterion, the effects of the indenter angle and tip radius are quantitatively explained. Our simulations suggest that the commonly used maximum principal fracture criterion might not be sufficient to describe fully the indentation fracture mechanism in brittle oxide glasses.

Results

Indentation with different indenter angles. The simulation setup is illustrated in Fig. 1. Detailed information can be found in the Methods section. As shown in Fig. 2, we conduct indentation simulations with indenter angles of 30°, 60° and 90°. The tip radius is atomically sharp. Under each indenter, a region with high tensile σ_{xx} stress is developed. Note that median crack usually occurs right under the indenter along the symmetry line, where σ_{xx} is also the principal stress σ_1. The indenter with a larger indenter angle pushes the tensile region away from the indenter tip. Pile-up is seen under the 60° indenter and 30° indenter during loading. For the 90° indenter, apparent pile-up occurs only after unloading (not shown). Under the 30° indenter, a small crack was nucleated, which can be more clearly seen in the close-up view around the indenter (in the upper-right part of Fig. 2). Using the 60° and 90° indenters, no crack is seen within 36 nm of the indentation depth, which is in agreement with previous studies using similar indenter geometry[27,30]. We will quantitatively explain why the crack can or cannot be nucleated in Section "Applying the fracture criterion to impact indentation".

Indentation with different tip radius. As shown in Fig. 3, for the same indenter angle (30°), indentation simulations are carried out with indenter tip radius ranging from atomically sharp (0.3 nm) to 6.5 nm. Under each indenter geometry, a region with high tensile σ_{xx} stress is developed, within which a median crack is eventually nucleated. From the close-up view around the indenter, we can see that under the 2 nm tip-radius and 3.5 nm tip-radius indenters, median crack is nucleated within 36 nm indentation depth. Under the indenter with tip-radius larger than 4 nm, no crack is seen within this 36 nm of indentation depth. Therefore the sample dimension in z direction is doubled to accommondate an indentation depth of 100 nm, and a median crack is nucleated at the indentation depth of 57 and 96 nm for the 5 and 6.5-nm tip radius indenters, respectively. Hence, we see that a larger indenter tip-radius tends to require a larger indentation depth in order to nucleate a median crack. Equivalently, the fracture load increases with tip-radius as shown in Fig. 3(b). A linear relationship between the critical load and tip radius is expected if self-similarity is perfectly obeyed. The slight slope change for larger samples in Fig. 3(b) might be caused by the excess confinement from the width of the sample due to the fact that the indentation depth is increased by more than 100% but the sample width is only increased by 30% (110 nm) due to computational cost. More simulations are certainly needed to explain such details. Another detail is that all the median cracks are nucleated sub-surface. With a larger indenter tip radius, the crack nucleation site will be farther away from the tip of the indenter.

The local fracture criterion. To understand the different crack nucleation behavior caused by various indenter geometries, we first need to understand the *local* fracture criterion. The locality is defined by a length scale over which the stress state can be regarded as homogeneous. As shown in Fig. 4(a), a search for the local fracture stress states is carried out using an independent set of simulations under homogeneous loading. To mimic the stress state in a thick sample and to be consistent with the indentation simulation, we consider the plain strain condition, and hence only two degrees of freedom exist, i.e., σ_1 and σ_2, which represent the first and

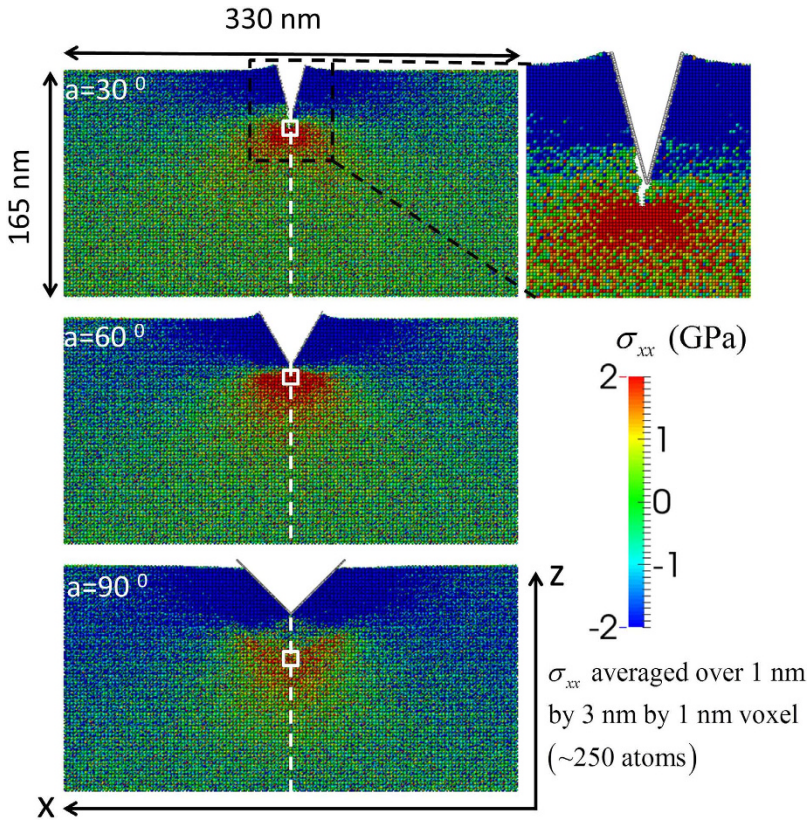

Figure 2. The deformation morphology and σ_{xx} stress field under an indentation depth of 36 nm with labeled indenter angle. A close-up view around the indenter and the nucleated crack under the 30° indenter is shown on the right. The local stress is averaged over the voxel of 1 nm by 3 nm by 1 nm, following the method described in a previous study[54]. Positive (negative) stress means tensile (compressive). The atoms in the indenter are colored gray. The symmetry line is indicated by the white dashed line. The maximum tensile site, i.e. the site with the largest σ_{xx} or σ_1, is schematically indicated by the white square for each sample. Note that with a larger indenter angle, the maximum tensile site is farther away from the indenter tip. The evolution of the full stress state at the maximum tensile site is discussed in Section "Applying the fracture criterion to impact indentation".

second principal stresses in the plain respectively. In the $\sigma_1 - \sigma_2$ domain, the compression dominant stress state is excluded since crack cannot be nucleated there. Along the path of $\sigma_1 = \sigma_2 = 1$ is the equal-biaxial tensile state, where a crack is bound to be nucleated at some stress level. Along the path of $\sigma_1/\sigma_2 = -1$ is the pure shear stress state. In between, the ratio of σ_2/σ_1 is tuned from -1 to 1 in steps of 0.2. In the other quarter of the space from $\sigma_1/\sigma_2 = -1$ to 1, the fracture criterion can be obtained by symmetry since the glasses are isotropic. In this way, the fracture stress states can be obtained along the loading paths covering the whole tensile-dominant domain.

In Fig. 4(b), we show the stress-strain curves and the corresponding final deformation morphologies. Brittle fracture happens from $\sigma_2/\sigma_1 = 1$ to 0 as the stress-strain curves abruptly drop to zero. Ductile failure happens for $\sigma_2/\sigma_1 = -0.2$. For σ_2/σ_1 from -0.4 to -1, the glass crosses over the ultimate tensile stress and enters into the flow state. Up to 40% strain, no fracture is observed. Note the sample length used here is 54 nm, much longer than the minimal sample length to avoid artificial ductility[31,32]. We also repeat the calculation in samples with lengths up to 200 nm and observe the same result. Therefore, the brittle-to-ductile transition observed here is a true material property and is not caused by having an artificially small sample size.

In Fig. 4(c), we map the loading trajectories in the $\sigma_1 - \sigma_2$ domain. The slope changes from -1 to 1 as is dictated by the loading. The stress state corresponding to the brittle fracture stress state is denoted by red crosses. If the glass enters into flow state, the ultimate yield point (the outmost stress state) is denoted by black circles. Passing the ultimate yield point, the stress states along different paths become effectively constant, fluctuating around the corresponding fixed stress states, i.e. the flow stress states as can be seen in Fig. 4(b). Since when $\sigma_2/\sigma_1 = -0.2$, a ductile failure occurs, we use both a red cross and black circle at the ultimate yield point. On the right, we show only the boundary points for σ_2/σ_1 from -1 to 1 and those obtained by symmetry for σ_1/σ_2 from -1 to 1. These boundary points form a locus, which we term the fracture criterion or fracture locus. The fracture criterion is the material property that determines the crack nucleation behavior. Although the fracture criterion is obtained under homogeneous loading condition, it is applicable to the *local* stress state in a non-homogeneous stress field since we can always define a scale within which a uniform stress state can be assumed.

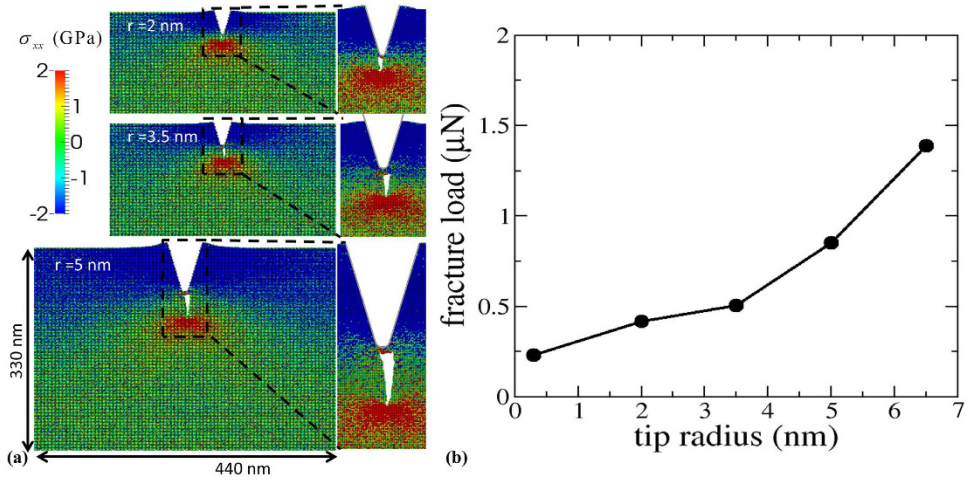

Figure 3. (**a**) The deformation morphology and σ_{xx} stress field using indenters with varying indenter tip radius. The close-up views around the indenter and the nucleated crack are shown on the right. The local stress is averaged over the voxel of 1 nm by 3 nm by 1 nm, following the method described in a previous study[54]. Positive (negative) stress means tensile (compressive). The atoms in the indenter are colored gray. Since indenter with the tip radius of 5 nm requires a larger indentation depth to nucleate a crack, a larger sample size is used. The evolution of the full stress state at the maximum tensile site is discussed in Section "Applying the fracture criterion to impact indentation". (**b**) The fracture load as a function of tip radius.

Applying the fracture criterion to impact indentation: The crack nucleation map. In Fig. 5, we apply the fracture criterion obtained in Fig. 4 to the indentation simulations with different indenter geometries. In Fig. 5(a), we track the stress state evolution of the maximum tensile site under the indenter with indenter angles of 30, 60 and 90°. The maximum tensile site is illustrated by the white box in Fig. 2. Note that maximum tensile site is not a physically fixed point in the sample. As the indenter depth increases, it moves further into the glass. For the 90° indenter, the maximum tensile site is effectively loaded under a very compressive state with σ_2/σ_1 to be about -2. For most of the time, the maximum tensile site is pinned at the flow state near $\sigma_1 = 2.5$ GPa and $\sigma_2 = -5$ GPa, as is illustrated by the gray dashed circle in Fig. 5(a). It is clear that such flow stress state is far away from the fracture stress states (red crosses), and therefore no crack is nucleated. When the indenter angle is reduced to 60°, the loading path of the maximum tensile site is rotated counter-clockwise in the principal stress domain, approaching to the more tensile direction and towards the fracture stress states. The flow state at the maximum tensile site is very close to the pure shear stress state with σ_2/σ_1 to be about -1. However, it is still away from the fracture stress states. For the 30° indenter, the stress state at the maximum tensile site steers towards the fracture stress state in the $\sigma_2/\sigma_1 = 0.4$ direction. Once the trajectory touches the fracture line, a crack is nucleated. After the crack nucleation, the maximum tensile site is at the crack tip and the stress state fluctuates around the point (7 GPa, 3 GPa). Therefore, we can see that the fracture criterion can quantitatively explain the effect of indenter angle in terms of crack nucleation behavior. Although the exact trajectory of the maximum tensile site is a function of elastic and plastic properties of the glass, the general trend should be true for most glasses that an indenter with a sharper indenter angle will increase the σ_2/σ_1 ratio for the maximum tensile site, thereby giving a greater probability of crack nucleation.

In Fig. 5(b), we apply the fracture criterion to the indentation with indenter angle of 30° and the tip radius of 2 nm. At the beginning when the indentation depth is very small, the glass can only sense the blunt tip but not the sharp indenter angle; therefore the maximum tensile site follows a direction of σ_2/σ_1 that is very negative, similar to that under the uniaxial compression loading condition. As the indentation depth increases, the effect of the sharp angle gradually becomes dominant, pushing the stress state of the maximum tensile site towards the direction of $\sigma_2/\sigma_1 = 0.4$, which is the direction an atomically sharp 30° indenter would enforce as shown in Fig. 5(a). The trajectory eventually reaches the fracture locus, which leads to crack nucleation. It is interesting to note that once the crack forms, the stress state at the crack tip is nearly the same for all of the simulations, including both loading and unloading. Similar scenarios are observed in all of the simulations with different indenter tip radii, as shown in Fig. 5(b–d). For a larger tip radius, a larger indentation depth is required to allow the effect of the indenter angle to take over, a direct result of the particular indenter geometry.

Discussion

From the above analysis, we see that one key factor in the fracture criterion is the transition ratio of σ_2/σ_1 at which flow behavior transitions to brittle fracture. For the current glass, the critical ratio is between -0.2 and 0, as shown in Fig. 4(a). It is expected that if the critical ratio of σ_2/σ_1 is reduced, the crack nucleation resistance would decrease dramatically and crack can be nucleated by blunter indenters. Therefore, the critical ratio of σ_2/σ_1 can be an important material index for contact damage resistance.

The loading rate is known to have an effect on the indentation fracture behavior[6] . In Fig. 6 (a), we show the fracture loci under different strain rates that span two decades. It is observed that the fracture locus shrinks (or

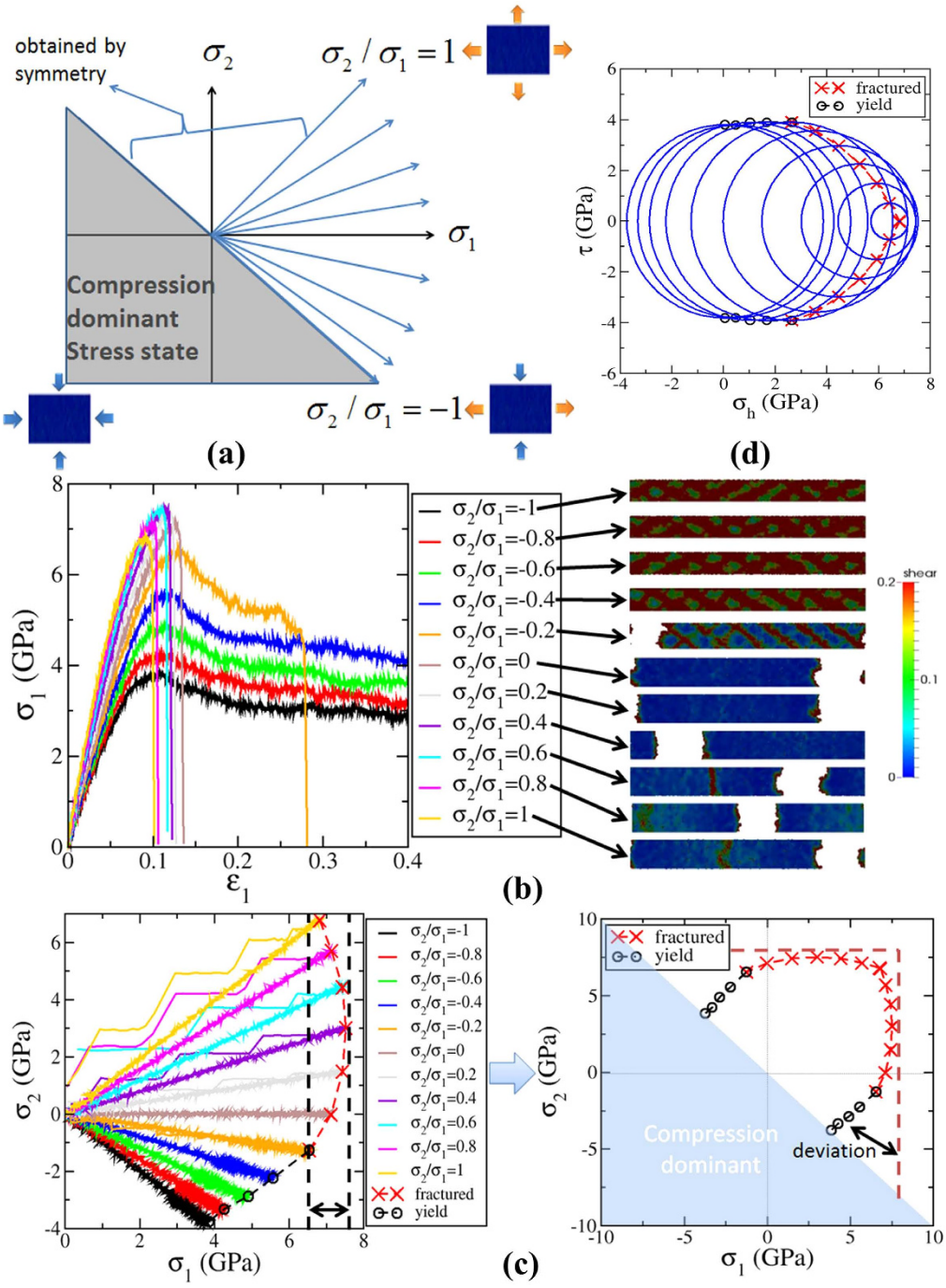

Figure 4. (**a**) An illustration of the strategy to search for fracture criterion in the principal stress domain. Loading path is tuned by the ratio of σ_2/σ_1. The compressive dominant domain is omitted. The upper quarter of space can be obtained by symmetry due to the isotropicity in glasses. (**b**) The stress strain curves for the ratio of σ_2/σ_1 from -1 to 1, in steps of 0.2. Corresponding final deformation morphologies, colored by atomic shear strain[56–58], are shown on the right. (**c**) The stress evolutions for the ratio of σ_2/σ_1 from -1 to 1 in the domain of σ_1 and σ_2. Red crosses collectively represent the crack nucleation stress states for the model glass under plain strain condition. Black circles denote the ultimate yield stress states, i.e., the maximum stresses the glass can reach before entering the flow state in (**b**). At the transition ratio of $\sigma_2/\sigma_1 = -0.2$, a ductile failure occurred, which is denoted by both a red cross and a black circle. Shown on the right, the crack nucleation stress states and the ultimate yield stresses form a locus, which is termed fracture locus. The fracture locus for σ_1/σ_2 from -1 to 1 was obtained by symmetry as illustrated in (**a**). Deviation from the maximum principal stress criterion is highlighted by the black double headed arrows. In the tensile regime, a maximum deviation of 1 GPa is seen. In the stress domain with one of the stresses to be compressive, significant deviation from the maximum principal stress criterion, both in the magnitude and in the brittle/ductile nature, is seen. (d) The equivalent fracture locus presented in the domain of the maximum shear stress $(\sigma_1 - \sigma_2)/2$ and in-plane hydrostatic stress $(\sigma_1 + \sigma_2)/2$. Blue circles are the Mohr circles for corresponding stress states.

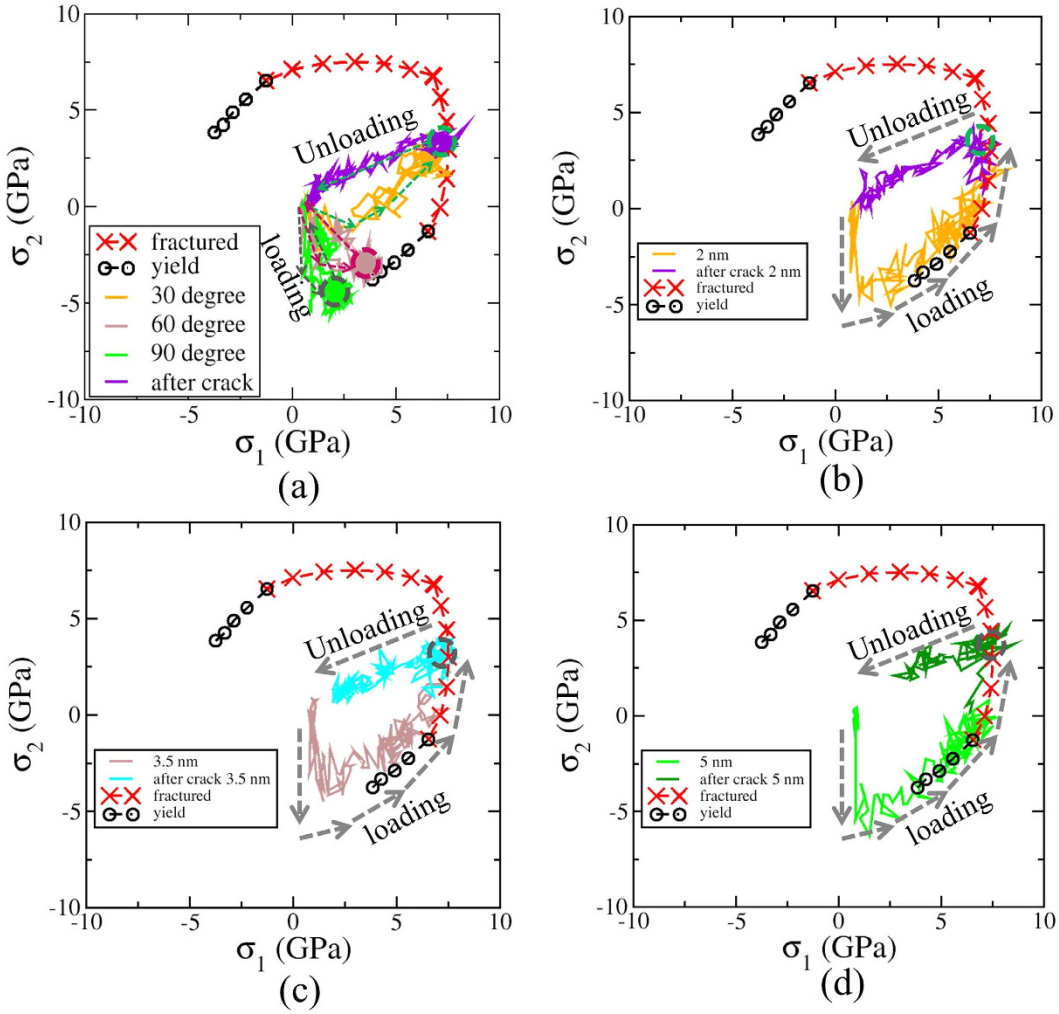

Figure 5. The fracture criterion and the stress state evolution of the maximum tensile site under different indenters, (**a**) for atomically sharp indenters with different angle and (**b–d**) for indenters with different tip radius. The dashed arrows indicate the direction of evolution. The dashed circles indicate the "fixed point", which is the local flow state for the simulations where no crack forms or the crack tip stress state for the simulations where crack forms. The stress state fluctuation is due to the fact that the maximum tensile site is very small, defined as 2 nm by 3 nm by 2 nm voxel containing around 1000 atoms. For each simulation where a crack is nucleated, the stress state evolution is colored differently after the crack nucleation event to show clearly that the transition state is close to the fracture criterion. For those simulations without crack nucleation, the stress state fluctuates around the flow state.

expands) when we decrease (or increase) the strain rate by one order of magnitude. In Fig. 6(b), we show the fracture stresses under different loading conditions as a function of strain rate. The fracture stress appears to decrease with strain rate in a Arrhenius manner. Therefore, it is important to confirm that the fracture criterion applied to indentation fracture in Fig. 5 is measured under a comparable strain rate. The effective strain rate experienced by the maximum tensile site under the indenter can be decomposed in to the product of the spatial stress gradient along the symmetry line and the speed of the indenter: $\frac{\partial\sigma_1}{E\partial t} = \frac{\partial\sigma_1}{E\partial z}\frac{\partial z}{\partial t} = \frac{\partial\sigma_1}{E\partial z}v$, where v is the speed of the indenter, E is the Young's modulus (measured to be 70.6 GPa) and z axis and the symmetry line are labeled in Fig. 2. The stress gradient can be estimated by the maximum stress (around 8 GPa) divided by the length scale of stress concentration (around 30 nm which can be seen Fig. 2). Solving this equation, we can estimate the effective strain rate experienced by the crack nucleation site to be 0.38 ns^{-1}. Therefore, it matches the strain rate we use to measure the fracture locus (0.4 ns^{-1}), and we can confirm that we have applied the appropriate fracture locus in Fig. 5. In reality, the relevant speed of impact is around 5 m/s when a hand-held device is dropped from a height of one meter. And the indenter depth is on the order of microns. Accordingly, the effective strain rate under the indenter is around 0.01 μs^{-1}. In Fig. 6(b), the relevant fracture stress will be lowered by 1 GPa as can be estimated from the extropolation. At longer time scale as in quasi-static indentation experiment, the effects of water is expected to further decrease the critical stress for crack nucleation[6,33]. Also, due to the effect of micro-flaws[34], crack propagation (rather than crack nucleation) can be made possible for indenters blunter than the ones studied here. However, we would like to emphasize that the presence of flaws will not affect the applicability of our local

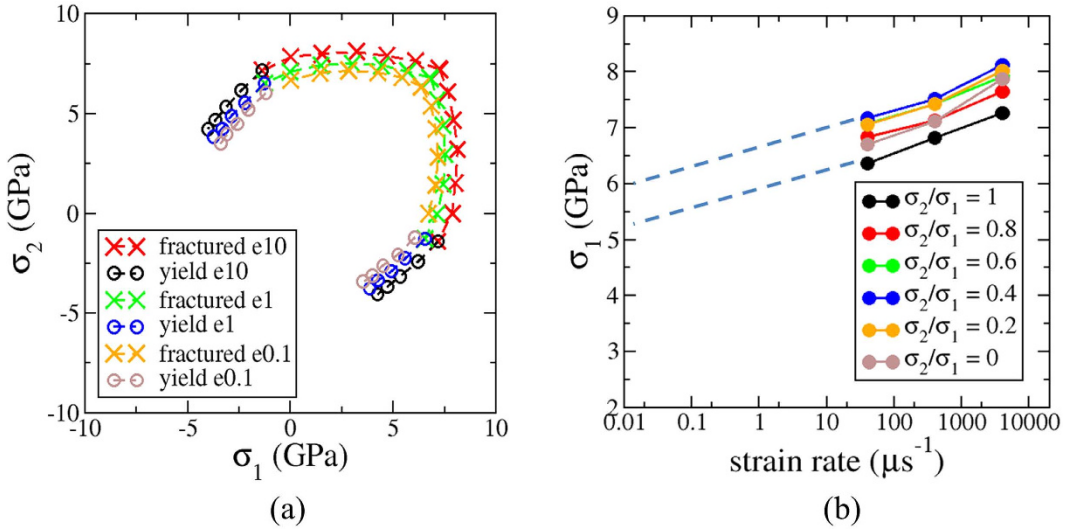

Figure 6. (**a**) The fracture loci at different strain rates that span two decades. e1 stands for 0.4 ns^{-1}, e10 stands for 4 ns^{-1} and e0.1 stands for 0.04 ns^{-1}. Fracture locus shrinks with decreasing strain rate. (**b**) The fracture stresses in (**a**) along different loading paths as a function of strain rate. The strain rate is shown in a log scale.

fracture locus. As shown in Fig. 5, when crack opens up, the stress state at the crack tip still satisfies the fracture locus. It is also very interesting to note that in experiment at macroscopic scale, median crack can be caused by shear localization and then shear faults under blunt indenters[6,21]. According to our previous study, shear band to crack transition has a length scale beyond nano-scale[24] even in metallic glasses which are much more prone to form a shear band. Shear band in oxide glasses are much less ready to occur due to less pronounced shear softening. Therefore shear banding and shear band to crack transition in oxide glasses might require a much larger sample size that is beyond nanoscale or submicron scale. As a result, shear faults or shear bands have not been observed in oxide glasses in MD simulations[27,28,30]. Further studies on these extrinsic factors are underway.

One important implication of this study is that the widely used maximum principal stress fracture criterion for brittle materials might not be sufficient for indentation fracture in glasses. As shown in Fig. 4(c), when both σ_2 and σ_1 are tensile, a deviation of 1 GPa exists between the observed and the maximum principal stress fracture criterion. More fundamental differences show up when one of σ_2 and σ_1 is compressive (which is a shear dominant stress state). The influence of shear stress can be seen in the equivalent fracture locus in Fig. 4(d). Shear dominant stress state is typical at the maximum tensile site under the indenter as can be seen in Fig. 5. Due to the presence of the shear dominant stress state, non-negligible shear or plastic deformation occurs under the indenter. A noticeable plastic zone and even shear bands have been observed in oxide glasses in experiments[6,22,33]. Plastic flow induced pile-up is also observed in current and previous MD simulations[27,30] and in nano-indentation experiments[8,9,35–37]. As shown in Fig. 5, for $\sigma_2/\sigma_1 < 0.4$ where the shear stress component increases, the fracture stresses decrease. This is in agreement with previous simulations[24] and experimental observations[6] that shear faults or shear flow can dramatically decrease the fracture stress. Moreover, below the critical ratio of σ_2/σ_1, plastic flow, instead of brittle fracture, occurs locally, rendering the fracture criterion based on maximum principal stress alone not sufficient. Our current MD simulations suggest that to achieve accurate prediction of indentation fracture, both in-plane principal stresses are required under plane strain condition and all three principal stresses might be required under general stress state. In the shear or compressive dominant stress state, local ductility should also be considered even for brittle glasses.

Conclusion

In summary, based on MD simulations we have developed a crack nucleation map in the principal stress domain to quantitatively explain the crack nucleation behavior under impact indentations with different indenter angle and indenter tip radius. The primary idea of the map is to decompose the complicated indenation fracture problem into two components. The first component is the local fracture criterion, which is an intrinsic material property that is mostly controlled by the glass composition and loading rate. The second component is the stress evolution of the maximum tensile site under indentation, which is controlled mostly by extrinsic parameters such as the indenter geometries. It is also affected by the elastic/plastic properties[37,38] of the glass, which will be discussed in future studies. In the map, the effect of indenter angle manifests itself as the ratio of the two in-plane principal stresses at the maximum tensile site, such that an indenter with sharper angle can push the stress state at the maximum tensile site towards the direction with larger σ_2/σ_1 where crack nucleation can happen, while an indenter with larger angle can only pin the stress state to the flow state with more negative σ_2/σ_1 that is far away from the fracture criterion. For the same indenter angle, a larger indenter tip radius will delay the increase of σ_2/σ_1 at the maximum tension site, thus requiring a larger indentation depth or load for crack nucleation. Due to the large shear or compressive stress component under indentation, the commonly held maximum principal stress fracture criterion might not be sufficient even for brittle glasses under indentation.

Methods

The Pedone force field[39] is used to simulate a silicate glass from the potassium end-member in the series of standard Na-K aluminosilicate glasses[35] with the mol % composition of $(Na_2O)_1(K_2O)_{14}(MgO)_5(Al_2O_3)_{10}(SiO_2)_{70}$. The force field has been used in previous MD studies to simulate the mechanical properties of oxide glasses[40–42]. A slab sample made of approximately 20000 atoms with random coordinates is equilibrated at 3000 K for 2 ns in an NVT ensemble (constant number of atoms, constant volume, and constant temperature)[43]. Then the high temperature melt is quenched to 300 K continuously over a period of 6 ns in an NVT ensemble. Finally, the glass is relaxed at 300 K under atmospheric pressure for 1 ns. The final dimension of the sample was 8.6 nm by 3 nm by 8.6 nm. Periodic boundary conditions are applied in all directions.

The simulation setup is illustrated in Fig. 1. Following previous MD studies[24,27,32,44], we replicate the small slab sample in x and z directions to make the sample large enough for mechanical testing. The periodicity in the replicated sample will be cancelled by the non-homogeneous stress field under the indenter[44]. A vacuum is introduced above the sample in z direction to accommodate the atomic indenter. Since the surface effect is negligible in the submicron-sized sample, we do not need to relax the surface before indentation and therefore save computational time. The atoms within 0.5 nm of the surface on the opposite boundary in the z direction are fixed throughout the indentation simulation to serve as the substrate. Periodic boundary conditions are still applied to the x and y directions. The thickness in the y direction is fixed at about 3 nm to mimic plain strain condition. For an indentation depth in the z direction of 36 nm, the dimensions of the large slab are about 330 nm by 3 nm by 165 nm (13 million atoms). We keep the width of the sample at least 4 times larger than the maximum width of the indentation impression and the depth of the sample 4 times larger than the maximum indentation depth. In this way, for the indenters with angles ranging from 30° to 90°, the stress field does not interact strongly with the boundary (see Figs 2 and 3). The indenter consists of carbon atoms, interacting with the glass via a repulsive force field for high energy collision[45]. The indenter itself is modeled as a perfectly rigid body so that no deformation is allowed in the indenter. In a 135 nm by 3 nm by 54 nm sample containing 1.8 million atoms, we conduct simulation with 5 m/s to 100 m/s to an indentation depth of 12 nm. We find that the evolution of the maximum principal stress under the indenter is almost the same. Therefore, to save computational time in the large samples, we use the indentation speed of 100 m/s. For the indentation depth of 72 nm with the indenter angle of 30° and the tip radius of 5 nm, the sample dimension (see Fig. 3) in the z direction is increased to 330 nm and the dimension in the x direction is increased to 440 nm (containing 35 million atoms). During indentation, the average temperature of the whole sample is maintained at 300 K in an NVT ensemble. For all the simulations, a time step of 2 fs is used[39]. The damped shifted force (dsf) method[46], which is an updated Wolf's method[47], was used to speed up the calculation of electrostatic interactions. The cutoff in the dsf method was chosen to be 8 Å and the damping parameter was set to be 0.25 $Å^{-1}$, consistent with the recipe[48]. We compared the results obtained by the dsf method and standard PPPM[49] method in terms of elastic moduli, hardness, and fracture toughness. The differences are within 3%. Therefore we deem that the dsf method employed here is appropriate for the mechanical properties of interest in this study. For other properties that are more sensitive to the cutoff in the electrostatic interaction, a longer cutoff or more sophisticated methods might be required[50–53]. The local stress is calculated following our previous study[54]. First, virial stress (in energy units) is calculated for each atom without being divided by atomic volume since the atomic volume in a glass is usually hard to define accurately. Then, the atoms are spatially partitioned in a through-thickness grid with a in plane resolution of 1 nm^2. The atomic stresses in each grid are summed and divided by the volume of the grid to yield the local stresses for each grid. All the simulations were conducted using LAMMPS[55].

References

1. Ostojic, P. & McPherson, R. A review of indentation fracture theory: its development, principles and limitations. *IJFr* **33,** 297–312, doi: 10.1007/BF00044418 (1987).
2. Lawn, B. & Wilshaw, R. Indentation fracture: principles and applications. *JMatS* **10,** 1049–1081, doi: 10.1007/BF00823224 (1975).
3. Cook, R. F. & Pharr, G. M. Direct Observation and Analysis of Indentation Cracking in Glasses and Ceramics. *J. Am. Ceram. Soc.* **73,** 787–817, doi: 10.1111/j.1151-2916.1990.tb05119.x (1990).
4. Johnson, K. L. *Contact Mechanics*. 1st edn, (Cambridge University Press).
5. Lawn, B. R. Indentation of Ceramics with Spheres: A Century after Hertz. *J. Am. Ceram. Soc.* **81,** 1977–1994, doi: 10.1111/j.1151-2916.1998.tb02580.x (1998).
6. Lawn, B. R., Dabbs, T. P. & Fairbanks, C. Kinetics of shear-activated indentation crack initiation in soda-lime glass. *JMatS* **18,** 2785–2797, doi: 10.1007/BF00547596 (1983).
7. Gross, T. M. Deformation and cracking behavior of glasses indented with diamond tips of various sharpness. *J. Non-Cryst. Solids* **358,** 3445–3452, doi: 10.1016/j.jnoncrysol.2012.01.052 (2012).
8. Smedskjaer, M. M., Mauro, J. C., Kjeldsen, J. & Yue, Y. Microscopic Origins of Compositional Trends in Aluminosilicate Glass Properties. *J. Am. Ceram. Soc.* **96,** 1436–1443, doi: 10.1111/jace.12298 (2013).
9. Kjeldsen, J. *et al.* Mixed alkaline earth effect in sodium aluminosilicate glasses. *J. Non-Cryst. Solids* **369,** 61–68, doi: 10.1016/j.jnoncrysol.2013.03.015 (2013).
10. Kassir-Bodon, A. *et al.* Raman Mapping of the Indentation-Induced Densification of a Soda-Lime-Silicate Glass. *International Journal of Applied Glass Science* **3,** 29–35, doi: 10.1111/j.2041-1294.2012.00078.x (2012).
11. Perriot, A. *et al.* Raman Microspectroscopic Characterization of Amorphous Silica Plastic Behavior. *J. Am. Ceram. Soc.* **89,** 596–601, doi: 10.1111/j.1551-2916.2005.00747.x (2006).
12. Niu, Y.-F., Han, K. & Guin, J.-P. Locally Enhanced Dissolution Rate as a Probe for Nanocontact-Induced Densification in Oxide Glasses. *Langmuir* **28,** 10733–10740, doi: 10.1021/la300972j (2012).
13. Tran, H., Clément, S., Vialla, R., Vandembroucq, D. & Rufflé, B. Micro-Brillouin spectroscopy mapping of the residual density field induced by Vickers indentation in a soda-lime silicate glass. *Appl. Phys. Lett.* **100,** 231901, doi: dx.doi.org/10.1063/1.4725488 (2012).
14. Hagan, J. T. Micromechanics of crack nucleation during indentations. *JMatS* **14,** 2975–2980, doi: 10.1007/BF00611482 (1979).
15. Lawn, B. R. Fracture and deformation in brittle solids: A perspective on the issue of scale. *J. Mater. Res.* **19,** 22–29 (2004).
16. Wondraczek, L. *et al.* Towards Ultrastrong Glasses. *Adv. Mater.* **23,** 4578–4586, doi: 10.1002/adma.201102795 (2011).
17. Imaoka, M. & Yasui, I. Finite element analysis of indentation on glass. *J. Non-Cryst. Solids* **22,** 315–329, doi: 10.1016/0022-3093(76)90062-4 (1976).

18. Giannakopoulos, A. E., Larsson, P. L. & Vestergaard, R. Analysis of Vickers indentation. *IJSS* **31,** 2679–2708, doi: 10.1016/0020-7683(94)90225-9 (1994).
19. Zeng, K., Giannakopoulos, A. E. & Rowcliffe, D. J. Vickers indentations in glass—II. Comparison of finite element analysis and experiments. *AcMeM* **43,** 1945–1954, doi: 10.1016/0956-7151(94)00393-V (1995).
20. Zhang, W. & Subhash, G. Finite element analysis of interacting Vickers indentations on brittle materials. *Acta Mater.* **49,** 2961–2974, doi: 10.1016/S1359-6454(01)00198-7 (2001).
21. Gross, T. M. & Tomozawa, M. Fictive temperature-independent density and minimum indentation size effect in calcium aluminosilicate glass. *J. Appl. Phys.* **104,** 063529, doi: 10.1063/1.2985907 (2008).
22. Gross, T. M. & Tomozawa, M. Indentation-induced microhardness changes in glasses: Possible fictive temperature increase caused by plastic deformation. *J. Non-Cryst. Solids* **354,** 4056–4062, doi: 10.1016/j.jnoncrysol.2008.05.042 (2008).
23. Abraham, F. & Gao, H. How Fast Can Cracks Propagate? *Phys. Rev. Lett.* **84,** 3113–3116, doi: 10.1103/PhysRevLett.84.3113 (2000).
24. Luo, J. & Shi, Y. Tensile fracture of metallic glasses via shear band cavitation. *Acta Mater.* **82,** 483–490, doi: 10.1016/j.actamat.2014.09.008 (2015).
25. Ken-ichi, N. *et al.* Interaction and coalescence of nanovoids and dynamic fracture in silica glass: multimillion-to-billion atom molecular dynamics simulations. *J. Phys. D: Appl. Phys*. **42,** 214011 (2009).
26. Bauchy, M. *et al.* Fracture toughness of calcium–silicate–hydrate from molecular dynamics simulations. *J. Non-Cryst. Solids* **419,** 58–64, doi: 10.1016/j.jnoncrysol.2015.03.031 (2015).
27. Yuan, F. & Huang, L. Brittle to Ductile Transition in Densified Silica Glass. *Scientific Reports* **4,** doi: 10.1038/srep05035 (2014).
28. Kilymis, D. A. & Delaye, J. M. Nanoindentation of pristine and disordered silica: Molecular Dynamics simulations. *J. Non-Cryst. Solids* **382,** 87–94, doi: 10.1016/j.jnoncrysol.2013.10.013 (2013).
29. Chen, Y.-C. *et al.* Interaction of Voids and Nanoductility in Silica Glass. *Phys. Rev. Lett.* **99,** doi: 10.1103/PhysRevLett.99.155506 (2007).
30. Nomura, K.-i., Chen, Y.-C., Kalia, R. K., Nakano, A. & Vashishta, P. Defect migration and recombination in nanoindentation of silica glass. *Appl. Phys. Lett.* **99,** 111906, doi: 10.1063/1.3637052 (2011).
31. Yuan, F. & Huang, L. Molecular dynamics simulation of amorphous silica under uniaxial tension: From bulk to nanowire. *J. Non-Cryst. Solids* **358,** 3481–3487, doi: 10.1016/j.jnoncrysol.2012.05.045 (2012).
32. Shi, Y., Luo, J., Yuan, F. & Huang, L. Intrinsic ductility of glassy solids. *J. Appl. Phys.* **115,** 043528, doi: 10.1063/1.4862959 (2014).
33. Gross, T. M. & Tomozawa, M. Crack-free high load Vickers indentation of silica glass. *J. Non-Cryst. Solids* **354,** 5567–5569, doi: 10.1016/j.jnoncrysol.2008.09.015 (2008).
34. Lawn, B. R. & Evans, A. G. A model for crack initiation in elastic/plastic indentation fields. *JMatS* **12,** 2195–2199, doi: 10.1007/BF00552240 (1977).
35. Kjeldsen, J., Smedskjaer, M. M., Mauro, J. C. & Yue, Y. On the origin of the mixed alkali effect on indentation in silicate glasses. *J. Non-Cryst. Solids* **406,** 22–26, doi: 10.1016/j.jnoncrysol.2014.09.036 (2014).
36. Rouxel, T., Ji, H., Guin, J. P., Augereau, F. & Rufflé, B. Indentation deformation mechanism in glass: Densification versus shear flow. *J. Appl. Phys.* **107,** 094903, doi: 10.1063/1.3407559 (2010).
37. Sellappan, P. *et al.* Composition dependence of indentation deformation and indentation cracking in glass. *Acta Mater.* **61,** 5949–5965, doi: 10.1016/j.actamat.2013.06.034 (2013).
38. Rouxel, T. Driving force for indentation cracking in glass: composition, pressure and temperature dependence. *Philosophical Transactions of the Royal Society of London A: Mathematical, Physical and Engineering Sciences* **373** (2015).
39. Pedone, A., Malavasi, G., Menziani, M. C., Cormack, A. N. & Segre, U. A New Self-Consistent Empirical Interatomic Potential Model for Oxides, Silicates, and Silica-Based Glasses. *The Journal of Physical Chemistry B* **110,** 11780–11795, doi: 10.1021/jp0611018 (2006).
40. Vargheese, K. D., Tandia, A. & Mauro, J. C. Molecular dynamics simulations of ion-exchanged glass. *J. Non-Cryst. Solids* **403,** 107–112, doi: 10.1016/j.jnoncrysol.2014.07.025 (2014).
41. Tandia, A., Vargheese, K. D. & Mauro, J. C. Elasticity of ion stuffing in chemically strengthened glass. *J. Non-Cryst. Solids* **358,** 1569–1574, doi: 10.1016/j.jnoncrysol.2012.04.021 (2012).
42. Tandia, A., Vargheese, K. D., Mauro, J. C. & Varshneya, A. K. Atomistic understanding of the network dilation anomaly in ion-exchanged glass. *J. Non-Cryst. Solids* **358,** 316–320, doi: 10.1016/j.jnoncrysol.2011.09.034 (2012).
43. Nosé, S. A unified formulation of the constant temperature molecular dynamics methods. *The Journal of Chemical Physics* **81,** 511, doi: 10.1063/1.447334 (1984).
44. Shi, Y. & Falk, M. L. Stress-induced structural transformation and shear banding during simulated nanoindentation of a metallic glass. *Acta Mater.* **55,** 4317–4324, doi: 10.1016/j.actamat.2007.03.029 (2007).
45. Ziegler, J. & Biersack, J. in *Treatise on Heavy-Ion Science* (ed. D. Allan Bromley) Ch. 3, 93–129 (Springer US, 1985).
46. Zahn, D., Schilling, B. & Kast, S. M. Enhancement of the Wolf Damped Coulomb Potential: Static, Dynamic, and Dielectric Properties of Liquid Water from Molecular Simulation. *The Journal of Physical Chemistry B* **106,** 10725–10732, doi: 10.1021/jp025949h (2002).
47. Wolf, D., Keblinski, P., Phillpot, S. R. & Eggebrecht, J. Exact method for the simulation of Coulombic systems by spherically truncated, pairwise r−1 summation. *The Journal of Chemical Physics* **110,** 8254–8282, doi: 10.1063/1.478738 (1999).
48. Demontis, P., Spanu, S. & Suffritti, G. B. Application of the Wolf method for the evaluation of Coulombic interactions to complex condensed matter systems: Aluminosilicates and water. *The Journal of Chemical Physics* **114,** 7980, doi: 10.1063/1.1364638 (2001).
49. Greengard, L. & Rokhlin, V. A Fast Algorithm for Particle Simulations. *J. Comput. Phys.* **135,** 280–292, doi: 10.1006/jcph.1997.5706 (1997).
50. Fanourgakis, G. S. An extension of Wolf's method for the treatment of electrostatic interactions: application to liquid water and aqueous solutions. *J. Phys. Chem. B* **119,** 1974–1985, doi: 10.1021/jp510612w (2015).
51. Lamichhane, M., Gezelter, J. D. & Newman, K. E. Real space electrostatics for multipoles. I. Development of methods. *J. Chem. Phys.* **141,** 134109, doi: 10.1063/1.4896627 (2014).
52. Takahashi, K. Z., Narumi, T. & Yasuoka, K. Cutoff radius effect of the isotropic periodic sum and Wolf method in liquid-vapor interfaces of water. *J. Chem. Phys.* **134,** 174112, doi: 10.1063/1.3578473 (2011).
53. Chen, Y. G. & Weeks, J. D. Local molecular field theory for effective attractions between like charged objects in systems with strong Coulomb interactions. *Proc Natl Acad Sci USA* **103,** 7560–7565, doi: 10.1073/pnas.0600282103 (2006).
54. Luo, J. & Shi, Y. The local stress state of a running shear band in amorphous solids. *J. Mater. Res.* **30,** 1979–1987, doi: 10.1557/jmr.2015.141 (2015).
55. Plimpton, S. Fast Parallel Algorithms for Short-Range Molecular Dynamics. *J. Comput. Phys.* **117,** 1–19, doi: 10.1006/jcph.1995.1039 (1995).
56. Falk, M. Molecular-dynamics study of ductile and brittle fracture in model noncrystalline solids. *PhRvB* **60,** 7062–7070, doi: 10.1103/PhysRevB.60.7062 (1999).
57. Shi, Y. & Falk, M. Atomic-scale simulations of strain localization in three-dimensional model amorphous solids. *PhRvB* **73,** doi: 10.1103/PhysRevB.73.214201 (2006).
58. Luo, J., Dahmen, K., Liaw, P. K. & Shi, Y. Low-cycle fatigue of metallic glass nanowires. *Acta Mater.* **87,** 225–232, doi: 10.1016/j.actamat.2014.12.038 (2015).

Acknowledgements
We are grateful for stimulating discussions with Bin Zhang, Petr Gorelchenko, Yu Xiao, Vijay Subramanian, Yongjian Yang, Liping Huang, and Yunfeng Shi. We are also grateful for the support from Matthew McKenzie, Christopher Wilson and ByoungSeon Jeon in the Scientific Computing group at Corning Incorporated and the Center for Computational Innovations (CCI) at Rensselaer Polytechnic Institute.

Author Contributions
J.M. and G.H. initiated and supervised the project at Corning. J.L. designed and conducted the simulations. K.D.V., J.M. and A.T. helped to set up the simulation. All authors discussed the results. J.L. wrote the manuscript. All authors reviewed and revised the manuscript.

Additional Information
Competing financial interests: The authors declare no competing financial interests.

How to cite this article: Luo, J. *et al.* Crack nucleation criterion and its application to impact indentation in glasses. *Sci. Rep.* **6**, 23720; doi: 10.1038/srep23720 (2016).